Langmuir probe analysis for high density plasmas

Francis F. Chen[a)]
Electrical Engineering Department, University of California, Los Angeles, California 90095-1594

(Received 14 December 2000; accepted 28 February 2001)

High-density, radio-frequency plasmas used in semiconductor processing have progressed to densities $n \geqslant 5\times10^{11}\,\mathrm{cm}^{-3}$, where the methods used to interpret Langmuir probe characteristics in low-density ($10^{9-11}\,\mathrm{cm}^{-3}$) plasma reactors are no longer valid. Though theory and computations for arbitrarily dense collisionless plasmas exist, they are difficult to apply in real time. A new parametrization and iteration scheme is given which permits rapid analysis of Langmuir probe data using these theories. However, at high *n*, measured ion saturation curves are shown which do not agree in shape with the ''correct'' theory, yielding anomalously high values of *n*. The discrepancy with independent measures of *n*, which can exceed a factor of 2, is believed to be caused by charge-exchange collisions well outside the sheath. Probe designs for avoiding this discrepancy are suggested. © *2001 American Institute of Physics.* [DOI: 10.1063/1.1368874]

I. BACKGROUND

A majority of the critical steps in the fabrication of a computer chip now involve plasma processing. The standard capacitive discharges used for these processes are gradually being replaced by so-called high density plasmas, particularly inductively coupled plasmas (ICPs) and helicon wave plasmas, which are both driven by radio-frequency power. These sources are capable of increasing the plasma density *n* from the $10^{9-11}\,\mathrm{cm}^{-3}$ range to the order of $5\times10^{12}\,\mathrm{cm}^{-3}$. In the low density regime, it is common practice in the industry to use the orbital motion limited (OML) theory of ion collection. This theory can be applied successfully well outside its intended range, but its error is greatly enhanced at high densities. Although a suitable theory exists, it is normalized in such a way that the result must be known before the calculation is begun. In this paper we present a method for parametrizing the theoretical curves so that fast, real-time analysis of probe curves at any density can be made with modern computers. This paper will treat only cylindrical probes, since spherical ones are impractical. Except at the end, collisions will be neglected because in high density plasmas the sheaths are much thinner than the mean free path. Attention will be focused on saturation ion currents, which present the most difficult problems.

The OML theory of ion collection was developed by Mott-Smith and Langmuir,[1] who found that the ion current to a negatively biased probe is independent of the shape of the plasma potential $V(r)$ as long as the current is limited only by the angular momentum of the orbiting ions. This required either the arbitrary assumption of a ''sheath edge'' *s*, beyond which the ion energy distribution was Maxwellian, or a $V(r)$ varying so slowly that no ''absorption radius'' inside of which all ions are drawn in exists between the probe and infinity. This condition is never satisfied even at modest densities. For $s\to\infty$ and a Maxwellian ion distribution at temperature T_i, the OML current to a cylindrical probe is given by

$$I = A_p j_r \left[\frac{2}{\sqrt{\pi}} \chi^{1/2} + e^{\chi}(1-\mathrm{erf}(\chi^{1/2})) \right]$$

$$\underset{\chi\gg1}{\to} A_p j_r \frac{2}{\sqrt{\pi}} \sqrt{1+\chi}, \tag{1}$$

where $\chi \equiv -eV_p/KT_i$, V_p is the probe voltage, A_p the probe area, and j_r the random thermal ion current. As $T_i\to0$, the T_i dependences of χ and j_r cancel, and a finite limiting value of the OML current exists:

$$I \underset{T_i\to0}{\to} A_p ne \frac{\sqrt{2}}{\pi} \left(\frac{|eV_p|}{M} \right)^{1/2}. \tag{2}$$

At the opposite extreme of dense plasmas and thin sheaths, ions enter the sheath with the so-called Bohm velocity

$$v_B = (KT_e/M)^{1/2}, \tag{3}$$

so that the saturation ion current is

$$I \approx \alpha ne A_p v_B, \tag{4}$$

independently of V_p, since the sheath adds very little to the probe radius R_p. Here, $\alpha n = n_s$ is the ion density at the sheath edge, with $\alpha\approx1/2$. The exact value of α depends on the conditions in the presheath, which can cause the ''saturation'' current to increase with V_p, even for a plane probe. Since the presheath thickness is generally $\geqslant R_p$, there is no simple way to treat a plane probe theoretically.

Between 1926 and 1957 many probe papers appeared, but all of them involved the arbitrary assumption of a sheath edge, since computers did not exist to handle the disparity in scale length between the sheath region and the quasineutral plasma region. In 1957 Allen, Boyd, and Reynolds (ABR)[2] derived a relatively simple differential equation which could be solved to give $V(r)$ for all *r* without division into sheath, presheath, and plasma regions. However, this theory was

a)Electronic mail: ffchen@ee.ucla.edu

only for spherical probes and only for $T_i=0$, so that ions moved radially into the probe, there was no orbital motion, and the absorption radius was at infinity. Chen[3] later extended the $T_i=0$ calculations to cylindrical probes. For finite T_i, ions with small angular momentum J would strike the probe and be collected, while those with large J would miss the probe and contribute twice to the ion density at any radius r which they reached. Thus, the density used to solve Poisson's equation for $V(r)$ depends on the current I, which is unknown. This difficult problem was solved by Bernstein and Rabinowitz (BR)[4] in 1959, but only for monoenergetic ions. The angular momentum forms an effective potential barrier for the ions, and those with sufficient energy E to overcome the barrier are collected. Thus, the constants of motion E, J determine the fate of each velocity class. In addition, $V(r)$ may have a local minimum in which ions can be trapped in closed orbits. Fortunately there has never been, to our knowledge, any indication of the existence of such a population of collisionally trapped ions. A simpler method, valid only for highly negative probes, was given by Lam,[5] who took advantage of the disparity in scale lengths at various radii. Using boundary layer techniques from aerodynamics, he derived a graphical method for computing ion currents. With modern computers, however, this method is no longer useful. Computations based on the ABR, BR, and Lam theories were given by Chen.[3,6] Experimental verification of the BR results was done by Chen *et al.*[7]

The BR computations were extended to Maxwellian distributions in the dissertation of Laframboise.[8] Since each velocity class (E,J) had its own idiosyncrasies, and there were convergence problems in the solution of the integral equations, these calculations were difficult and nontrivial. Unfortunately, only the cases $\beta\equiv T_i/T_e=0$, 0.5, and 1 were treated; if β had been taken to be 0.1, the results could have been used forthwith, without the nonuniform convergence problems in the case $T_i=0$. When $T_i\to 0$, one might expect the BR–Laframboise (BRL) results to reduce to the ABR results, but they do so only for spheres, not for cylinders. The reason is that as $r\to\infty$ while $T_i\to 0$, the angular momentum J takes the indeterminate form $\infty\times 0$, which is zero for spheres but finite for cylinders. By asymptotic analysis of the governing equations, Laframboise showed that this limit depends on whether $V(r)$ varies faster or slower than $1/r^2$. For cylinders, it varies more slowly, causing J to be finite even if $T_i=0$. Consequently, the ABR theory cannot be used for cylindrical probes; we must use the Laframboise curves or the BR results, which are only slightly different from each other for $\beta\ll 1$.

Further computations of this type were given later by Virmont and Godard,[9] but only for spherical probes. Numerous extensions of collisionless probe theory have been made; for instance, to collisional plasmas by Cohen,[10] to flowing plasma by Chung *et al.*,[11] and to magnetized plasmas by Stangeby.[12] However, the collisionless theories worked out in the 1960s are still state-of-the-art and are appropriate for high density, low pressure plasmas. These results, however, are normalized to units that depend on the variables to be determined and are therefore difficult to apply to the experiment.

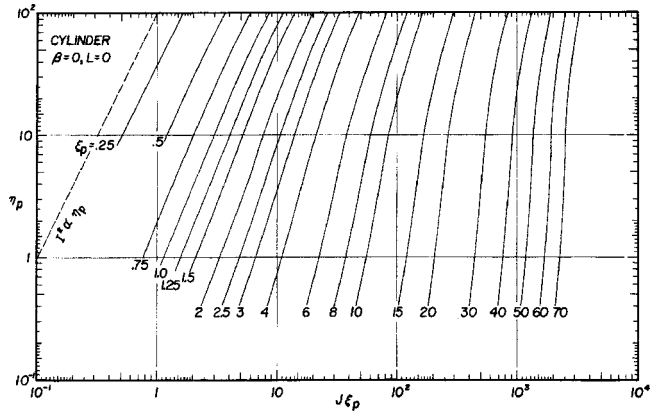

FIG. 1. Curves of ion saturation current for increasing plasma density (from Ref. 13). The abscissa is proportional to ion current, and the ordinate to the probe potential. The dashed line has the slope of OML theory: $I^2\propto V$.

II. PARAMETRIZATION OF LAFRAMBOISE CURVES

In 1965, Chen[13] showed that the apparent linearity of current–voltage (I^2-V) curves of ion current was fortuitous and unrelated to the OML formula of Eq. (2). For instance, this dependence is found in ABR theory, which has no orbital motions, and also for spherical probes, for which OML theory would predict a linear $I-V$ dependence. Figure 1, copied from that paper, shows ABR curves of ion current over a large range of ξ_p, where ξ_p (or, simply, ξ) is the ratio of probe radius to Debye length

$$\xi_p\equiv\xi\equiv R_p/\lambda_D, \quad \lambda_D\equiv(\epsilon_0 KT_e/ne^2)^{1/2}. \tag{5}$$

The slope of the curves at low ξ_p (low density) is indeed consistent with linear I^2-V, but the curves bend at high ξ_p (high density), approaching true ion saturation with constant I. Figure 2 shows the $I-V$ curves of Laframboise[8] for $T_i=0$ and various values of ξ. Since they cannot be easily recalculated, it is these curves that we wish to represent by analytic functions for arbitrary values of ξ and V_p. Following Ref. 8, we use the following normalizations:

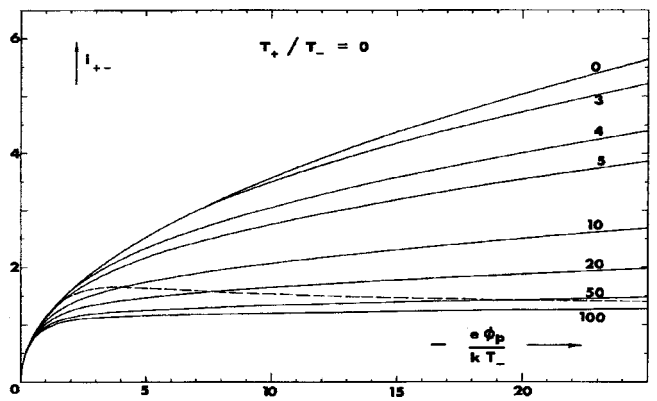

FIG. 2. Laframboise curves of normalized ion current vs normalized probe potential for $T_i=0$. The curves are labeled by the value of $\xi_p=R_p/\lambda_D$. (From Ref. 8, Fig. 40.)

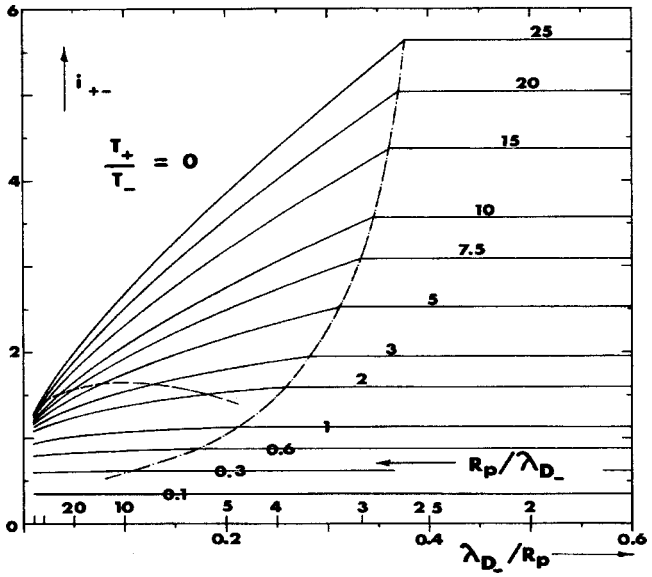

FIG. 3. Laframboise curves for ion current at low values of ξ (from Ref. 8, Fig. 43). Each curve is for constant η, and ξ is plotted on the abscissa from right to left.

$$\eta \equiv \eta_p \equiv -\frac{e(V_p - V_s)}{KT_e},$$
$$i = \frac{I_i}{I_0} = \frac{I_i}{enA_p}\left(\frac{KT_e}{2\pi M}\right)^{-1/2} \equiv \frac{I_i}{nJ_r}, \tag{6}$$

where V_p and V_s are the probe and space (plasma) potentials, I_i is the ion current to a cylindrical probe with area $A_p = 2\pi R_p L$, and J_r is a random ion current per unit density (evaluated at T_e). Equation (6) is invariant to the system of units, but it is convenient to express I_i and e in mks, with the other quantities in cgs. Note that η depends on V_s and T_e, and i on n, all quantities that are not known until the analysis is complete.

Steinbrüchel *et al.*[14,15] and Mausbach[16] have parametrized these curves with a two-parameter function of the form

$$i = A\eta^B, \tag{7}$$

but it is clear that the bend in the $I-V$ curves in Fig. 1 for large ξ cannot be represented by so simple a function. Instead, we have used the following four-parameter fitting function:

$$\frac{1}{i^4} = \frac{1}{(A\eta^B)^4} + \frac{1}{(C\eta^D)^4}, \tag{8}$$

where the parameters $ABCD$ are functions of ξ. The first term on the right in Eq. (8) is dominant for small η, giving an approximate $i^2 \propto \eta$ dependence, while the second term dominates at large η, where the slope is smaller. The ratio C/A determines where the bend in the curve occurs, and the exponent 4 affects the sharpness of the bend. Fortunately the same exponent could be used for all curves.

The parametrization proceeds in two stages. In stage 1, values of $ABCD$ are found which give good fits to the curves of Fig. 2 for the available values of ξ. In stage 2, functions $A(\xi)$, $B(\xi)$... are found so that the parameters $ABCD$ can be evaluated for arbitrary ξ. In stage 1, the curves of Fig. 2 were carefully digitized by direct measurement. For low values of η and ξ we used the expanded graph in Ref. 8, shown in Fig. 3. In addition to these graphs, Laframboise[8] gave the numerical values of the points which were actually computed. Since the curves were no doubt interpolated by a draftsman, in collecting the data set we gave extra weight to those points for which exact values were known. An example of a data set and the functional fit using Eq. (8) is shown in Fig. 4 on a log–log plot. The scatter in the points arises from errors in reading Figs. 2 and 3 because of the finite width of the lines. With four parameters ($ABCD$) to be varied in the least squares fit, a multiplicity of solutions could be obtained depending on the starting values. We first fit the slopes B and D to the left and right portions of the curve, respectively, and then adjusted the values of A and C to get an overall fit. Only then were all four parameters varied to get the final least squares minimization.

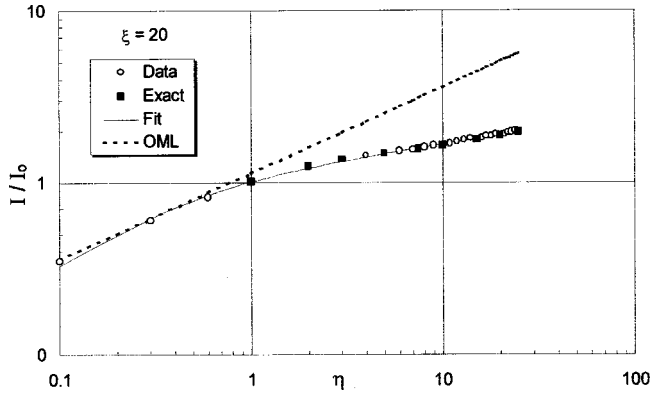

FIG. 4. Example of fitting Laframboise data (points) with a four-parameter function (line). The radius of the points is ≈2%. Points for which exact values were available are shown by the large squares. The orbital motion limit is shown by the dashed line.

The entire data set and the corresponding least squares fits are shown in Fig. 5. All available values of ξ are listed, but to avoid clutter some values are not plotted. The curve for $\xi=0$ agrees with the OML limit given by Eq. (2). Close examination of Fig. 5 will show that the slope changes dis-

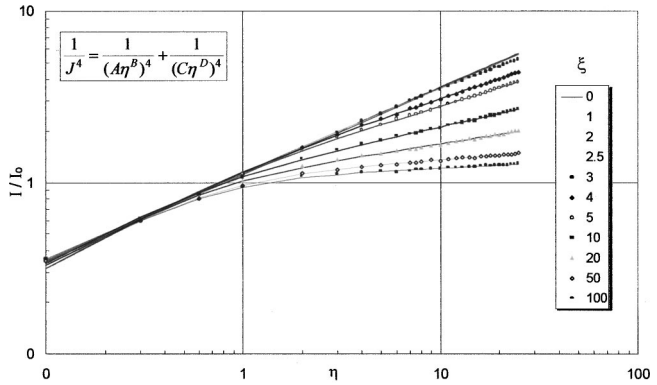

FIG. 5. The Laframboise data set (points) and analytic fits (lines) for all available values of ξ. The curves are in the same order as in the legend, but for clarity some curves are not drawn.

TABLE I. Fitting parameters used for the curves of Fig. 5.

ξ	A	B	C	D
0	1.585	0.451	1.218	0.526
1	1.453	0.477	1.233	0.517
2	1.445	0.494	1.224	0.514
2.5	1.412	0.531	1.255	0.486
3	1.142	0.541	2.146	0.316
4	1.433	0.646	1.306	0.378
5	1.513	0.670	1.244	0.351
10	1.473	0.635	1.166	0.257
20	1.384	0.622	1.104	0.181
50	1.203	0.544	1.095	0.091
100	1.181	0.532	1.067	0.055

continuously at $\xi=3$. This value of ξ separates the region ($\xi<3$) in which the OML limit is approximately valid from the region ($\xi>3$) where it is not. The physical meaning is that, for $\xi\geqslant 3$, the formation of an absorption radius begins to limit the probe current. Except for the point $\eta=0$, which has little experimental value, the fitting error over the entire range of η and ξ is less than $\approx 3\%$, and in most cases less than 1%–2%. The values of the parameters $ABCD$ used in Fig. 5 are shown in Table I; as explained above, this is by no means a unique set of values.

In stage 2, we attempt to express the parameters $ABCD$ as analytic functions of ξ. The values in Table I are plotted in Fig. 6(a). We see that all the curves have a discontinuity at $\xi=3$, except for the OML exponent B. These jumps are real;

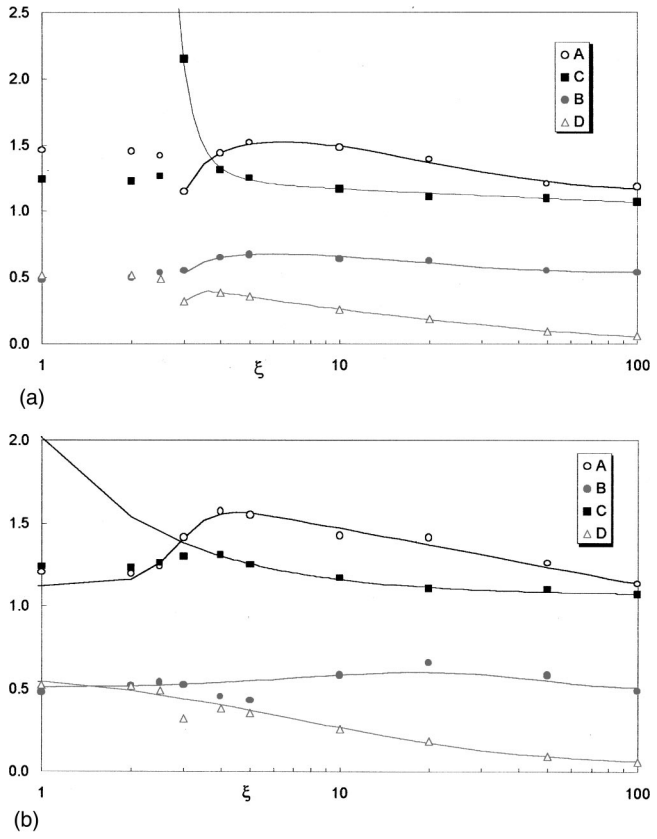

FIG. 6. The parameters A, B, C, and D for available values of ξ and analytic fits to them for: (a) $\xi>3$ and (b) all ξ.

TABLE II. Coefficients for calculating $ABCD(\xi)$ for $\xi>3$.

	a	b	c	d	f	g
A	1.142	19.027	3.000	1.433	4.164	0.252
B	0.530	0.970	3.000	1.110	2.120	0.350
C	0.000	1.000	3.000	1.950	1.270	0.035
D	0.000	2.650	2.960	0.376	1.940	0.234

attempts to smooth over them yielded poor results. More insight into this behavior can be seen from Fig. 3, where it is seen that the curves change discontinuously to a horizontal line near $\xi=3$. The reason for this is that for cylinders the BR theory converges poorly for small ξ, yielding currents larger than the OML limit. Laframboise argues that the ion current cannot exceed this limit because, when a thin sheath is formed, it shields the plasma from the probe potential, and ions cannot be drawn in from large distances. For lack of a better procedure, he arbitrarily cuts off the ion current when it reached the OML value. This limit is not observed in experiment. Laframboise[8] shows data by Sonin[17] which follow the extrapolation of the curves of Fig. 3 without an OML cutoff. This is physically reasonable, since any small collision far from the probe can change the angular momentum of an incoming ion. The obvious solution is to ignore the OML limit and use the extrapolation of the curves of Fig. 3. Unfortunately, the parameters $ABCD(\xi)$ then behave even more erratically than in Fig. 6(a), and we were unable to fit them to smooth functions.

The fitting of $ABCD(\xi)$ to analytic functions was carried out in two steps. In step 1, the values for $\xi<3$ were ignored, and the origin of the curves was shifted to $\xi=3$. The following functional forms were used:

$$A,B,D(\xi)=a+b(\xi-c)^d\exp[-f(\xi-c)^g],$$
$$C=a+b\exp[-c\ln(\xi-d)]+f(1-g\ln\xi). \tag{9}$$

Thus, each parameter A, B, C, or D, was fitted using six other parameters $abcdfg$, which we shall call *coefficients* to avoid confusion. Possible values for these are given in Table II. This is by no means a uniquely optimized set; we simply show that a set exists which can be used to reproduce the Laframboise curves accurately. Figure 6(a) shows the resulting curves of $ABCD(\xi)$, as analytic fits to the points in that figure. With these smoothed parameters, the calculated data points of Fig. 5 can be fitted within 3% down to $\xi=3$.

In step 2, we sacrifice accuracy in order to fit the parameters $ABCD(\xi_j)$ for all known values, ξ_j, of ξ. The parameters $ABCD$ are chosen not to give the best fit to the data but to give a reasonable fit while varying more smoothly as functions of ξ. Since C becomes large for $\xi<3$, the second term in Eq. (8) is negligible for small ξ. We therefore choose a function $C(\xi)$ which fits the points $\xi>3$ in Fig. 6 and which diverges rapidly for $\xi<3$. The function $D(\xi)$ is then immaterial for $\xi<3$ and needs to be fitted only for large ξ. Having chosen $C(\xi)$ and $D(\xi)$, we then fix C and D at their *smoothed* values while optimizing A and B. This results in a new set of parameters $ABCD$, given in Table III, which are

TABLE III. Degraded parameters for fitting the curves of Fig. 5.

ξ	A	B	C	D
0.1	1.141	0.496	1.218	0.526
1	1.199	0.477	1.233	0.517
2	1.194	0.515	1.224	0.514
2.5	1.234	0.537	1.255	0.486
3	1.415	0.522	1.294	0.316
4	1.568	0.446	1.306	0.378
5	1.546	0.422	1.244	0.351
10	1.426	0.583	1.166	0.257
20	1.415	0.654	1.104	0.181
50	1.255	0.583	1.095	0.091
100	1.130	0.486	1.067	0.055

to be fitted with new functions $A(\xi)$ and $B(\xi)$. The new set of functions, involving new coefficients $abcdf$, is as follows:

$$A = a + \frac{1}{\frac{1}{b\xi^c} - \frac{1}{d\ln(\xi/f)}},$$

$$B,D = a + b\xi^c \exp(-d\xi^f), \tag{10}$$

$$C = a + b\xi^{-c}.$$

Table IV gives the new coefficients, and Fig. 6(b) shows the points and fitting curves of step 2, valid for all ξ. In spite of the fact that the points in Fig. 6(b) are still erratic and the fits poor, the smooth curves in this figure yield $I-V$ curves agreeing with those in Fig. 2 to within $\approx 5\%$ for $0<\xi<100$. The largest discrepancies occur for $\xi \approx 4$–5, where both terms in Eq. (8) are significant. Again, we emphasize that the parameters of Table III are by no means optimized. By degrading the stage 1 fit using other local minima in the least-squares process, it may be possible to make the points $ABCD(\xi_j)$ lie on smoother curves that can be fitted more readily.

Comparison of the two parametrizations is shown for two sample values of ξ in Figs. 7(a) and 7(b) on log–log plots. Although it is not easy to see on this scale, the step 1 coefficients give closer fits than the step 2 coefficients. The largest discrepancies are for $\eta<1$, where the ion current is only a small contribution to the total current anyway. Note that the fits of Fig. 5 are better than those of Fig. 7 because the parameters $ABCD$ in Fig. 5 were not calculated from analytic functions.

Finally, we consider the effect of finite ion temperature. Figure 8 shows the Laframboise calculations[8] for i versus η at $\xi=10$ for various ratios T_i/T_e. Since in partially ionized gas discharges T_i rarely exceeds 0.1 eV, the correction for finite T_i is entirely negligible except for $\eta<1$.

TABLE IV. Coefficients for calculating $ABCD(\xi)$ for all ξ.

	a	b	c	d	f
A	1.12	0.00034	6.87	0.145	110
B	0.50	0.008	1.50	0.180	0.80
C	1.07	0.95	1.01	—	—
D	0.05	1.54	0.30	1.135	0.370

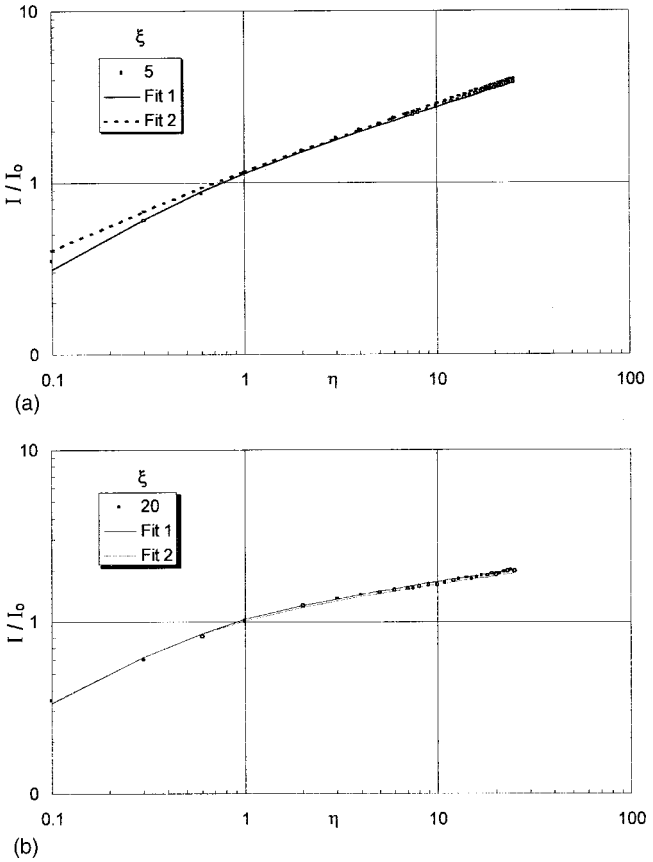

FIG. 7. Parametric fits to the Laframboise data for: (a) $\xi=5$ and (b) $\xi=20$. The points have a radius of 2%. The solid line (fit 1) shows the curve optimized for $\xi \geqslant 3$; the dashed line (fit 2), the curve optimized for all ξ.

III. ANALYSIS PROCEDURE

To obtain accurate values of n, T_e, and V_s (but not T_i) from the $I-V$ characteristic, the most difficult task is to separate the ion current I_i from the electron current I_e, and vice versa, in the region near the floating potential, where both contribute to the total current I. Now that we have accurate ion curves for small values of η, we can subtract I_i from I_e,

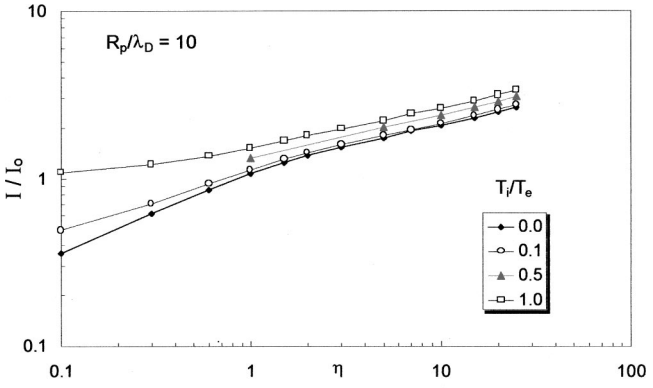

FIG. 8. Laframboise data for the variation of ion $I-V$ curves with ion temperature, at $\xi=10$.

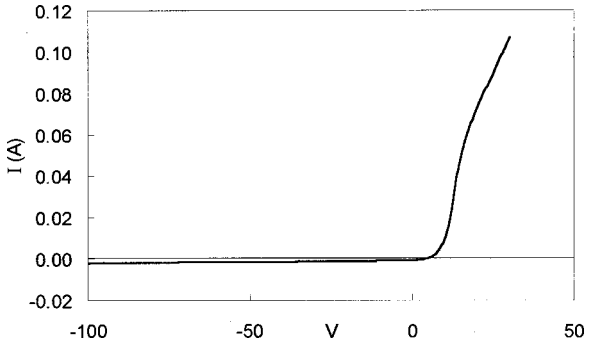

FIG. 9. Sample $I-V$ curve to be analyzed ($I_e>0$ here). The data were taken with an 0.15 mm diam, 1 cm long probe in a 900 W, 2 MHz ICP in 20 mTorr of argon. The density was of order $4\times10^{11}\,\mathrm{cm}^{-3}$, and KT_e was $\approx$2 eV.

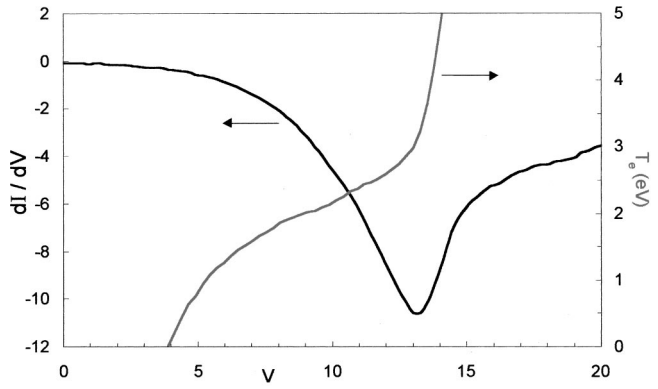

FIG. 10. Initial determination of V_s and T_e from derivative of the $I-V$ curve. Ion current is positive here.

and then I_e from I_i, in an iterative procedure. We shall illustrate this technique using data from an inductively coupled discharge in 10 mTorr of argon, taken with an rf-compensated probe of radius 0.075 mm and length 1 cm (Hiden ESPion®). A similar iterative scheme is used by Hopkins and Graham.[18]

Except in negative-ion plasmas, it is inadvisable to attempt to obtain the electron density n_e from the saturation electron current, although this has been done successfully in quiescent, field-free plasmas of very low density. There are several reasons for this. The space potential V_s, at which n_e is determined, is usually found from the inflection point of the $I-V$ curve or from the ''knee'' at which the extrapolated lines of the saturation and transition regions cross. This point is ill defined, and n_e depends exponentially on the choice of V_s. Magnetic fields and collisions can move the knee of the curve. Radio-frequency fluctuations can distort this particularly nonlinear part of the curve. Drawing large electron currents to the probe can also deplete the plasma or damage the probe. If n_i and n_e were to differ by as much as 0.1%, Poisson's equation shows that d^2V_s/dx^2 would be on the order of 200 V/cm^2, which is impossible outside of a sheath. Therefore, apart from low density ($n<3\times10^{10}\,\mathrm{cm}^{-3}$), rf-free plasmas, n_e is in principle best determined from the ion saturation current, assuming quasineutrality; and any disagreement between n_i and n_e[18,19] simply shows the error in measuring n_e. In the following procedure, we do not use electron saturation except for an initial estimate of n. However, it will be seen that there are still problems with the theories of ion collection.

A. Step 1

The current to the end area of the probe is subtracted out by dividing the measured probe current I by an aspect ratio factor A_r, defined by

$$S=2\pi R_pL,\quad A_r=(S+\pi R_p^2)/S=(1+R_p/2L). \tag{11}$$

Depending on the value of ξ, the end of the probe can collect from a hemispherical sheath or a plane one. Since the correction is small, we have simply assumed a small increase in the cylindrical area. The entire $I-V$ curve in this example is shown in Fig. 9.

B. Step 2

The data are smoothed to remove digital noise, and dI/dV is computed; the maximum of this gives a first estimate of the space potential V_s. This estimate will not affect the final determination of V_s, which is found from the ion and electron fits and the condition of quasineutrality. If the electron distribution is Maxwellian, the ratio $I/(dI/dV)$ yields a first estimate of T_e:

$$I_e\propto\exp[e(V_p-V_s)/KT_e],\quad \frac{I_e}{dI_e/dV_p}=\frac{KT_e}{e}, \tag{12}$$

which is T_e in eV. These curves are shown in Fig. 10, with T_e read directly from the right-hand scale. From the minimum in the dI/dV curve, the space potential is seen to be $\approx$13 V. Since the ion contribution to I_e has not yet been subtracted, the apparent T_e varies with V_p. Taking a potential $\approx2T_e$ more negative than V_s, we estimate T_e to be about 2.1 eV in this example.

C. Step 3

A rough estimate of plasma density n can be found from $I_e(V_s)$:

$$I(V_s)\approx I_e(V_s)=neS(KT_e/2\pi m)^{1/2}. \tag{13}$$

This yields a density of $\approx1.7\times10^{11}\,\mathrm{cm}^{-3}$. A second estimate can be found from the Bohm formula of Eq. (4) applied to the current at the most negative probe potential measured. Since the sheath has expanded at that potential, α should be given a value $\gg1/2$, perhaps 2. This yields a density of $\approx6\times10^{11}\,\mathrm{cm}^{-3}$. These estimates may differ considerably, but they are needed only to provide an order of magnitude.

D. Step 4

Having working values of V_s, T_e, and n, we can now evaluate λ_D, ξ, and J_r from Eqs. (5) and (6). The parameters $ABCD(\xi)$ can then be evaluated using Eq. (9) if $\xi\gg3$, or Eq. (10) if ξ is less than 3 or close to 3, together with Tables II and IV, respectively. Equation (10) can always be used but is somewhat less accurate.

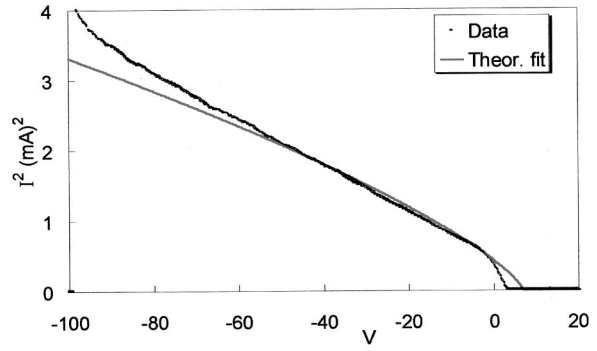

FIG. 11. Square of saturation ion current vs probe voltage as measured (dots) and as computed after optimization (smooth line).

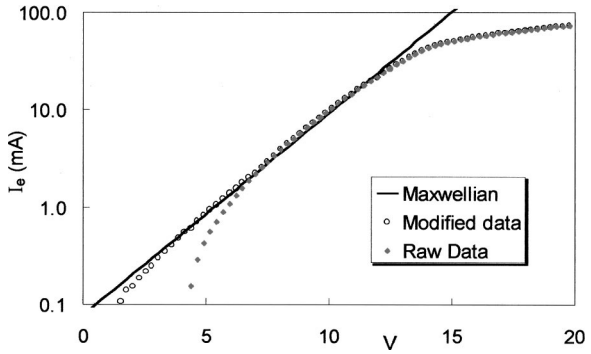

FIG. 12. Semilog plot of electron current as originally measured (diamonds) and after subtraction of ion component (circles). The line is a fit to a Maxwellian distribution.

E. Step 5

The theoretical ion current can now be found as a function of V_p from Eq. (6)

$$I_i = nJ_r i, \tag{14}$$

with i given by Eq. (8) as a function of η. Using the preliminary values of V_s and T_e, we can convert $I_i(\eta)$ into $I_i(V_p)$ using Eq. (6). The measured and calculated curves of I_i^2 are shown in Fig. 11. The reason that we plot $I_i^2 - V$ rather than $I_i - V$ is that measured $I_i^2 - V$ curves tend to be linear over a larger range of densities than one would expect from this theory.

F. Step 6

The values of n and V_s are then adjusted for a least squares fit to the data, avoiding the region near V_s. The value of n controls the magnitude of the curve, and the value of V_s its slope. The result is the thin line in Fig. 11. The discrepancy between theory and experiment near V_s is expected, since the contribution of electrons has not yet been subtracted. In general, the value of V_s given by this fit ($\equiv V_s^i$) will differ from that required to fit the electron current ($\equiv V_s^e$); this will be discussed later. Note that we do not vary T_e at this step. From Eq. (6), we see that i^2 and η both vary as T_e^{-1}, so that a fit of $i^2(\eta)$ is independent of T_e. Unfortunately, i depends weakly on T_e through the value of ξ, and iteration is necessary.

G. Step 7

Next, the *calculated* ion current is subtracted from the probe current to obtain the electron current. We do not subtract the *measured* ion current, since that contains an electron component. Figure 12 shows a semilogarithmic plot of I_e, as compared with the raw data. In this case, subtracting the ion current has greatly improved the linearity of this curve. The solid line is a graph of the equation

$$I_e = neS(KT_e/2\pi m)^{1/2} \exp[e(V_p - V_s^e)/KT_e] \tag{15}$$

using the value of n determined by the ion fit.

H. Step 8

A least squares fit of the I_e data is made by varying T_e and V_s^e, yielding the line shown in Fig. 12. The resulting value of V_s^e is the space potential required by quasineutrality, regardless of where the ''knee'' of the $I-V$ curve is located. For each trial value of T_e or V_s^e, ξ and η will change, and the ion curve has to be recalculated. The I_e data are then also recalculated because the ion subtraction has changed. Despite the complexity, these least square fits of a 500-point data set require less than 15 s on a 400 MHz computer using an uncompiled spreadsheet program. Since T_e has changed, the ion curve in Fig. 11 will no longer fit the data.

I. Step 9

Steps 4–8 are repeated until consistent values of n, T_e, V_s^i, and V_s^e are obtained. In this example, the result is $n = 5.15 \times 10^{11}\,\mathrm{cm}^{-3}$, $T_e = 2.09\,\mathrm{eV}$, $V_s^e = 14.9\,\mathrm{eV}$, and $V_s^i = 17.1\,\mathrm{eV}$.

J. Step 10

The electron current can now be subtracted from the ion data to give the true ion current. This can be done in two ways. If the ion-corrected electron current is subtracted, the result is shown in Fig. 13. If the *theoretical* electron current (assuming a Maxwellian distribution) is subtracted, the result

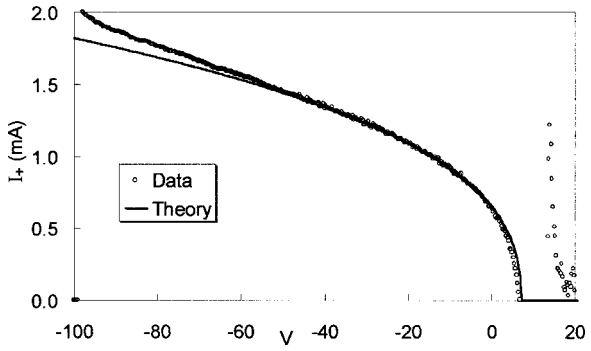

FIG. 13. Linear plot of saturation ion current after subtraction of corrected electron current. The line is the theoretical fit. The points at the right are electron currents which appear because of the mismatch between the space potentials assumed for the ion and electron fits.

TABLE V. Parameters for fitting the ABR curves.

	A	*B*	*C*	*D*
0.5	0.314	0.493	0.314	0.493
1	0.846	0.488	1.033	0.360
1.5	1.511	0.468	2.152	0.283
2.5	3.637	0.409	4.329	0.298
4	6.677	0.423	10.63	0.200
6	14.79	0.367	21.67	0.140
10	21.75	0.430	55.68	0.158
30	291.5	0.205	417.1	0.039
50	796.2	0.167	1113	0.008
70	1691	0.122	2110	−0.030

(not shown) has a discontinuity near V_s because of the discrepancy between V_s^e and V_s^i. Non-Maxwellian electrons would cause these curves to differ even more.

Some disagreement between V_s^e and V_s^i can be expected because: (a) the ion current for $\eta \approx 0$ cannot be calculated accurately, being sensitive to small perturbations and poor convergence; (b) it is fit least well by our analytic functions; and (c) it is furthermore sensitive to ion temperature (cf. Fig. 8). However, it is surprising that the discrepancy is so large and is not always of the same sign. This problem has not been encountered before, because no attempts had been made to evaluate I_i near $\eta=0$ accurately. Another possibility is that ion trapping in closed orbits is occurring at low potentials. However, Laframboise[8] points out that with cylindrical probes trapped ions can escape by moving parallel to the axis. As is evident from the erratic behavior of Fig. 13 near V_s, it is difficult to separate I_i and I_e near the space potential, and this may affect the apparent electron distribution function at low energies.

IV. ANALYSIS WITH OTHER PROBE THEORIES

It is apparent from our sample case (Fig. 11) that the BRL theory diverges from the experimental points at large negative voltages. As will be seen in Sec. VI, this discrepancy vanishes at low densities but becomes large at high densities. For this reason, we need to test the accuracy of the other available theories. Ion currents predicted by the OML theory are simply given by Eq. (2). The curves of the ABR theory, however, require parametrization. The procedure is essentially the same as that in Sec. II, and the details will be omitted. Since the bend in the ABR curves is opposite to that in the BRL curves (Fig. 5), the fitting function of Eq. (8) has been modified, and the normalized ion current i is replaced by $J\xi_p$, which is independent of n

$$J\xi_p = I_i R_p (e/KT_e)^2 (2MKT_e)^{1/2} = [(A\eta^B)^4 + (C\eta^D)^4]^{1/4}. \tag{16}$$

Here I_i is the ion flux, not current, per cm length, and cgs units are used. In practical units, Eq. (16) can be written

$$I_i(\mathrm{mA}) = 0.327 (J\xi_p) T_{eV} (n_{11}/A)^{1/2} L/\xi_p, \tag{17}$$

where n_{11} is n in units of $10^{11}\,\mathrm{cm}^{-3}$, A is the atomic number of the gas, and L the probe length in cm. The computed data to be fitted were taken from the original curves reproduced in Ref. 13, including Fig. 1 of the present paper. The parameters $ABCD(\xi)$ for the best fit to the ABR data are shown in Table V. These parameters are fitted with the following functions of ξ:

TABLE VI. Coefficients for calculating $ABCD(\xi)$ for ABR theory.

	a	*b*	*c*	*d*
A	0.864	1.500	0.269	2.050
B	0.479	−0.030	−0.010	—
C	1.008	1.700	0.336	2.050
D	0.384	−0.150	0.013	—

$$A, C = a\xi^b + c\xi^d, \qquad B, D = a + b\ln\xi + c(\ln\xi)^2. \tag{18}$$

The fitting coefficients $abcd$ are shown in Table VI.

The OML, BRL, and ABR theories predict different magnitudes and shapes for the ion saturation curves. This can be seen in Fig. 14, which compares the three theories with the same data used for the example of Figs. 9–13. It is seen that the OML curve fits the linear I^2-V dependence of the data almost exactly. The deviation of the data from this line at the highest voltages is in the ''wrong'' direction and is probably caused by secondary electron emission. The ABR curve fits the data well at low voltages but shows some saturation at high voltages. The BRL curve shows more saturation and does not follow an I^2-V dependence at all. As shown in the figure, each theory requires a different value of density in order to fit the data. In general, the BRL and OML theories agree at small values of ξ, as they should, since Laframboise[8] forced them to do so as explained in Sec. II. For large ξ, the data follow the OML curve much more closely than the BRL curve, even though the OML theory is not expected to be accurate for $\xi > 3$. Indeed, the BRL fit is so poor at large ξ that there is considerable latitude in choosing the combination of n and V_s^i that gives the best fit. In practice, we chose a combination that also straightens the $\ln I_e - V$ curve as much as possible. The ABR theory in general fits the *shape* of the data curves better than does the BRL theory; but, as we shall see, the resulting values of n are

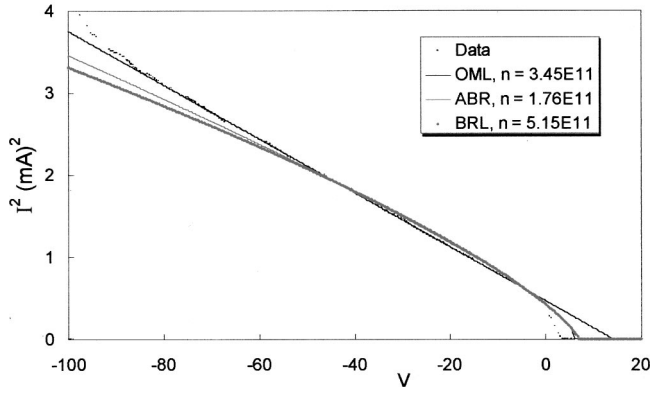

FIG. 14. Comparison of ion saturation data with the shapes of curves predicted by three probe theories. The densities required for the fits are shown in the legend. The value of ξ for this example is 5.0 for the BRL density and 4.1 for the OML density.

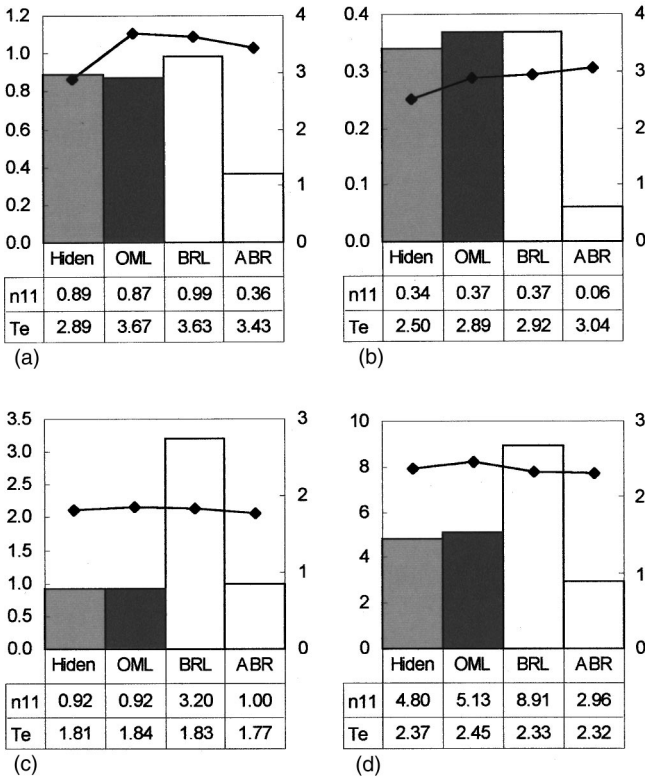

FIG. 15. Comparison of density and temperature values obtained from different methods of probe analysis for sample cases with ξ=(a) 1.1, (b) 3.1, (c) 4.6, and (d) 9.1.

too low to be realistic. When the OML theory is applicable, the values of V_s^e and V_s^i agree well, but for large ξ these values diverge because of the inaccuracy of the theories near the plasma potential. Usually the OML fit requires too large a value of V_s^i, while the BRL and ABR theories require too small a value of V_s^i.

V. COMPARISON OF THEORIES WITH EXPERIMENT

We have analyzed some 15 probe curves taken by Evans and Zawalsky[20] with various probe radii and plasma conditions in an ICP, using a Hiden ESPion® probe system. Experimental details are outside the scope of this paper and will be given in a separate paper. The values of KT_e are insensitive to the method of analysis used, but the densities n can vary by a factor of 3 or more from theory to theory, leading to a large uncertainty in the interpretation of the data. The discrepancy, however, follows a trend that can be discerned in the four cases chosen for illustration in Fig. 15. The bar marked ''Hiden'' is the density given by the ESPion® software package and differs from the OML result only because the value of KT_e involved a slightly different fit to the data. The values of KT_e, shown by the connected points, are almost the same for all methods, but the values of n differ by an amount which increases with $\xi = R_p/\lambda_D$. The BRL formalism consistently yields density values larger than the OML theory, while the ABR densities are always lower than the OML density.

The ABR theory, which neglects angular momentum and ion orbiting, overestimates the ion current to the probe, thus

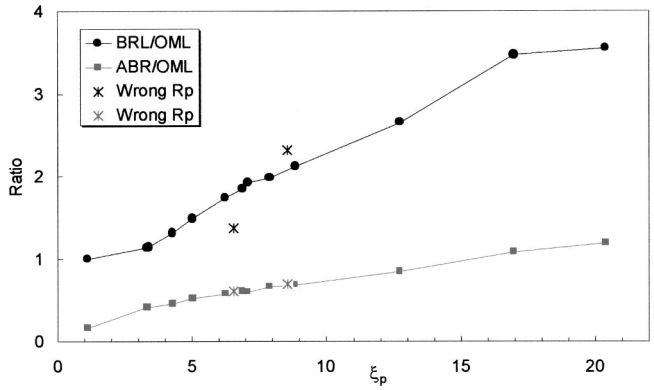

FIG. 16. Ratios of densities obtained with the BRL, OML, and ABR theories for test cases with varying values of ξ (computed with the BRL density). The starred points lying off the line were calculated assuming an incorrect probe radius.

underestimating the density. Since it accounts for an absorption radius, which the OML theory does not, it could have predicted a lower ion current and higher density than does the OML theory; but apparently the effect of angular momentum is larger, and the ABR density is always lower than the OML density. Although the BRL and OML theories both incorporate angular momentum, the OML formula neglects the formation of an absorption radius and allows the probe potential to attract ions from large distances, thus overestimating the current and underestimating the density. However, the BRL theory does not necessarily give the right answer, because it does not fit the shape of the ion $I-V$ characteristic as well as the OML theory does.

A comparison of the three theories for our test cases is shown in Fig. 16, which plots the BRL/OML and ABR/OML density ratios as functions of ξ. The BRL/OML ratio approaches unity as $\xi \to 0$, as expected, and increases monotonically with ξ. As ξ increases and the sheath becomes thin, the probe potential is shielded from distant points in the plasma, an effect neglected in OML theory. Hence, OML predicts too large a current and too small a density, the error increasing with ξ. To test the sensitivity to ξ, we analyzed two $I-V$ curves assuming an incorrect value of R_p, and hence of ξ. These cases are shown by the two points marked with a star (*) and lie well off the trend line of the other points. The ABR/OML ratio is usually below unity, for reasons stated above.

We believe that BRL theory is also inaccurate because it applies to strictly collisionless plasmas. In the presence of charge-exchange collisions in a gas like argon, the angular momentum of an incoming ion far from the probe can easily be destroyed by a collision, after which the ion will be accelerated radially by the probe's electric field. Enough angular momentum remains, however, for the current to be lower than that predicted by ABR theory. Our previous experimental check of BRL theory[7] was done in a thermionic Q-machine, which was fully ionized and gave large values of ξ because of the low temperature. There, the ion current was well saturated and fitted the shape of the BRL curves. In a partially ionized plasma, however, collisions well outside the sheath can change the angular momentum distribution so that

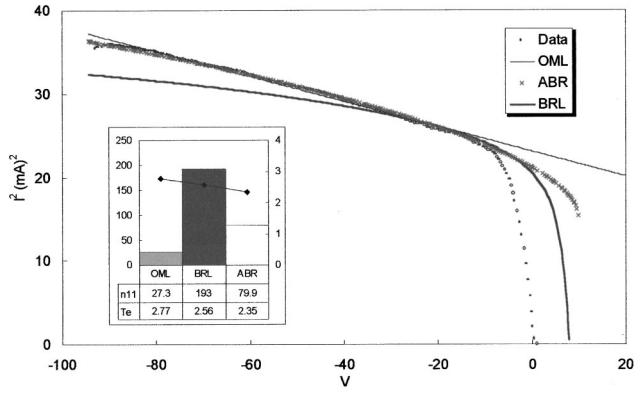

FIG. 17. Data from a high-density helicon plasma compared with three theoretical curves. The inset shows the values of n and T_e obtained from these fits. The 2 kW discharge was in 8 mTorr of argon with a 600 G magnetic field, and the probe was 0.3 mm in diameter.

the ion curves more closely follow the I^2-V dependence predicted by the OML theory and, to a lesser extent, the ABR theory.

Well saturated ion curves can also be obtained in a partially ionized plasma by using a large probe at high density. Figure 17 shows data from a helicon plasma in the $n=10^{13}\,\mathrm{cm}^{-3}$ range[21] attaining a value of $\xi=56$. Although not shown, the BRL/OML and ABR/OML density ratios fall on an extrapolation of the trend line in Fig. 16. The straight I^2-V line corresponding to the OML theory is clearly inappropriate, since it crosses the axis at 154 V, and an unreasonably low density has to be assumed to achieve the small slope of the curve. The ABR theory, however, fits the data quite well with a reasonable density, while the BRL curve has a lower slope than the data. In these fits, V_s^i has been adjusted so that the electron current is Maxwellian after the ion current has been subtracted. Near the floating potential, the data points in Fig. 17 fall below the theory because they have not yet been corrected for the electron contribution.

To compare the probe results with independent measurements of density, we have obtained preliminary data by Evans and Zawalsky[20] using microwave interferometry. Figure 18 shows these density measurements as a function of rf power P_{rf} in a commercial ICP, compared with probe-determined densities analyzed with the BRL and ABR theories. It is seen that there is reasonable agreement among all three methods at low P_{rf} (small ξ), but that at high P_{rf} (large ξ) the BRL density is too high, and the ABR density too low compared with the microwave determination. However, the geometric mean of the BRL and ABR densities (shown by the dotted line and starred points) agrees well with the microwave measurement and has the proper slope.

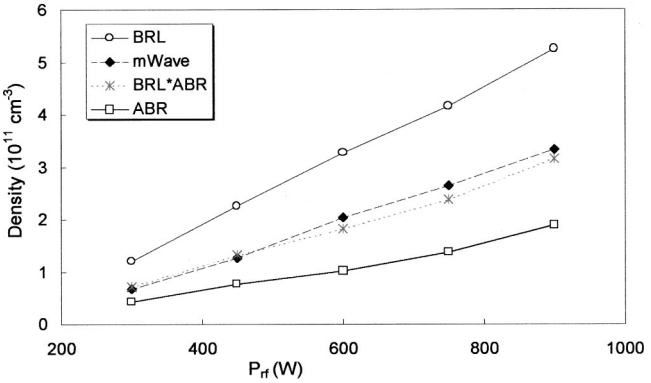

FIG. 18. Values of density vs ξ as obtained from the BRL and ABR theories, as compared with microwave measurements (♦). The stars (*) are the geometric mean between the BRL and ABR densities.

An exact treatment of the problem for partially ionized plasmas would require adding a collision term to the Bernstein–Rabinowitz formalism, but even then the results would depend on the pressure and species of the gas and would not be expressible in terms of universal curves. We have attempted to devise a hybrid technique, using the ABR theory for radii above a critical radius R_c, to account for the shielding of potentials by thin sheaths and the finite-sheath-thickness OML theory for $r<R_c$ to account for ion orbits in the collisionless region. For instance, one could choose R_c to be the mean free path, but this is usually well outside the sheath. Alternatively, one could choose R_c to be several Debye lengths larger than R_p, or to be the radius at which $\eta=\eta_c=1$. The ABR current would be calculated for a probe with $R_p=R_c$ and $\eta_p=1$, thus neglecting the ions' angular momenta in the exterior region. The OML current can then be calculated for a sheath edge at $r=R_c$ and a Maxwellian ion distribution there with $T_i \leqslant T_e$. Setting the two currents equal to each other should yield the value of R_c or η_c, whichever is the unknown. The process is repeated for each probe potential V_p. The density assumed initially would be adjusted and the process repeated until the curve agrees with the data. Unfortunately, our attempts to carry out this procedure failed.

VI. SUMMARY AND CONCLUSIONS

The proper use of probe theory for high density, partially and fully ionized plasmas is treated in this paper, which incorporates several distinct research results:

(1) A double parametrization technique has been developed to facilitate the use of the Laframboise and ABR computational results. This algorithm permits rapid generation of theoretical $I-V$ curves for arbitrary values of λ_D/R_p, leading to real-time analysis of probe data with fast portable computers.

(2) An iteration scheme is described which uses the parametrized curves to separate the ion and electron currents collected by the probe. Although this separation fails between the floating and space potentials because of inaccuracies in the theory, this method yields more accurate determinations of density and electron temperature than previously possible.

(3) Comparison with experiment reveals a dilemma: The OML (or ABR) theory fits the shape of the ion saturation curves better than the BRL theory in regimes where the OML (or ABR) theory should be inapplicable. The correct density, as determined by microwave interferometry, lies between those given by the BRL and OML (or ABR) theories. We surmise that the cause of the failure of the collisionless

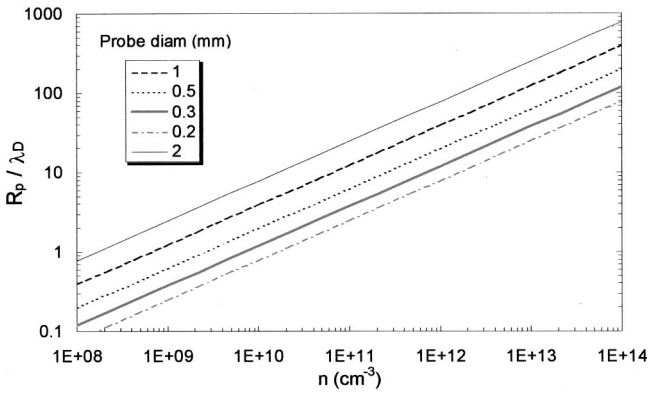

FIG. 19. Dependence of ξ on density, for $T_e=3$ eV and various probe diameters. The thick line is for $R_p=0.15$ mm, a common and convenient size which, however, gives an intermediate value of ξ in high density plasmas.

BRL and OML formalisms is neutral charge exchange, which destroys ion angular momentum far from the probe.

(4) In partially ionized plasmas, collisionless probe theories are inadequate for $3<\xi_p<100$, and density determinations can be in error by a factor of 2 or more. The correct density is bracketed by the predictions of the BRL and OML (or ABR) theories. For $\xi_p<3$, the OML theory can be used, since it agrees with the BRL theory in that range. For $\xi_p>100$, the ABR theory should be sufficiently accurate, since the sheath is so thin that ion orbiting would not be a problem. The ABR differential equation would have to be solved, however, since the parametrization in this paper was done only up to $\xi_p=70$. More simply, the Bohm formula can be used for large ξ_p. For intermediate values of ξ_p, it is found phenomenologically that the geometric mean of the BRL and ABR densities agrees with independent measurements, although there is no theoretical justification for this.

(5) In view of these results, the design of Langmuir probes for use in rf plasmas is discussed in Appendix A.

(6) For dense, fully ionized plasmas, straight-line extrapolation of the ion saturation curve is commonly used. The accuracy of this approach compared with the exact BRL curves is assessed in Appendix B. It is also shown there that the slope of the I_i-V curve is approximately 3/4.

ACKNOWLEDGMENTS

The author thanks W. Zawalski, J. D. Evans, and M. Light for sharing their data.

This work was partially supported by Applied Materials, Inc., the University of California Semiconductor Manufacturing Alliance for Research and Training (SMART), Plasma-Therm, Inc., and Hiden Analytical, Ltd.

APPENDIX A: PROBE DESIGN

Because of the effect of collisions for intermediate values of ξ, probes should have either very small or very large diameters to operate in regimes where collisionless theories can be trusted. Figure 19 shows values of $\xi_p=R_p/\lambda_D$ as a function of n for various probe diameters. One sees that a diameter of 0.2 mm or less can be used with the OML theory up to densities of $\approx 10^{11}\,\mathrm{cm}^{-3}$. For $n>10^{12}\,\mathrm{cm}^{-3}$, a 2-mm-diam probe can access the region $\xi_p>100$, and it should be long enough to resemble an infinite cylinder. One should not attempt to draw saturation electron current with such a probe! In the density range $10^{11-12}\,\mathrm{cm}^{-3}$, it is difficult to choose a probe size for which an existing theory gives the correct result in a weakly collisional plasma. However, the $I-V$ curve of a thick probe can sometimes be successfully analyzed using a modified Bohm formula (Appendix B).

In regimes where the theory is good, determination of the probe area is a limiting factor in the accuracy of Langmuir probe measurements. The probe radius can change from ion sputtering, either during measurement or during discharge cleaning of the surface. Short probes have end collection which is difficult to account for. If the insulating ceramic is too large, plasma may creep into into it, extending the probe length; and if it is too narrow, the probe tip may make electrical contact with conducting films deposited on the ceramic. To minimize the interference of the probe with the plasma, the mounting hardware near the probe tip should be no larger than 2 mm in diameter.

In reactive ion etchers, ICPs, and helicon sources used in semiconductor processing, there are large fluctuations in V_s at the rf frequency. It is well known[22] that this can greatly distort the $I-V$ characteristics. Many methods of rf compensation have been published, but the most successful seem to be the use of tuned inductors close to the probe tip, in conjunction with a nearby floating electrode which is ac coupled to the probe to drive V_p in synchronism with the rf fluctuations.[19,23] The area of the floating electrode should be large enough to drive the probe tip but small enough to give spatial resolution; a criterion is given below. In plasma sources with insulating walls, insertion of a large grounded electrode is necessary to serve as a reference for V_p. A floating double probe cannot be used in this situation because the entire assembly does not float at the rf frequency unless extraordinary means are used to drive its stray capacitance. Furthermore, the rf compensation of each tip would have to be identical. Since rf oscillations tend to decrease the floating potential V_f, one can compare rf compensation schemes by observing how positive a value of V_f is obtained. However, because of stray capacitances, one can never be sure of measuring V_f correctly by terminating the probe in a high resistance. The safest way to measure V_f is to terminate in a low resistance and detect the zero crossing of the probe current.

A criterion for designing the auxiliary floating electrode was given by Sudit and Chen.[23] The probe tip P is coupled to the oscillating space potential $\tilde{V}_{\mathrm{rf}}$ through a sheath capacitance C_s, given approximately by

$$C_{s,x}=\frac{1}{2^{7/4}}\frac{\epsilon_0 A_{s,x}}{\lambda_D}\left[\frac{e(V_s-V_p)}{KT_e}\right]^{-3/4}, \tag{A1}$$

where A_s is the sheath (or probe) area. The capacitance C_x of an auxiliary electrode of area A_x coupled to the probe tip at point P is given by the same formula. The corresponding impedances $|Z_{s,x}|$ are $1/\omega C_{s,x}$. For the probe tip to follow $\tilde{V}_{\mathrm{rf}}$, the effective impedance $Z_{L\,\mathrm{eff}}$ of the isolating inductors, Z_L, must be large compared with the larger of $|Z_{s,x}|$. $Z_{L\,\mathrm{eff}}$ is

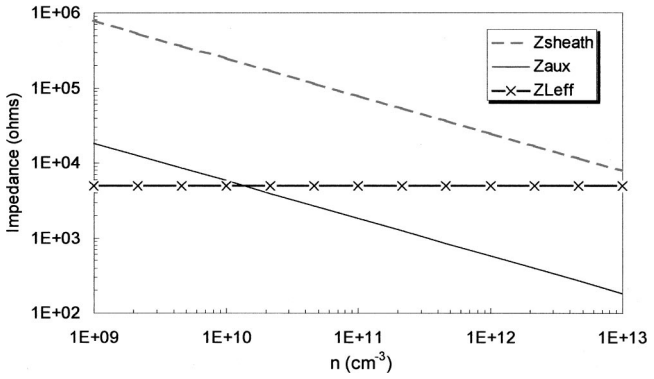

FIG. 20. Example of design of auxiliary electrode for rf compensation. $Z_{\rm aux}$ (—) should be well below $Z_{L\ \rm eff}$ (×) for the density measured. $Z_{\rm sheath}$ (— — —) is the sheath impedance without an auxiliary electrode. The conditions assumed were: $KT_e=3$ eV, $R_p=0.075$ mm, $L=1$ cm, $f=2$ MHz, $A_x=2$ cm^2, and $Z_L=250\,\mathrm{k}\Omega$.

the parallel combination of Z_L and the stray impedance to ground of the short wire between P and the chokes. For instance, a 1 cm long wire has a capacitance to ground of $\approx$0.25 pF, and the stray impedance at 2 MHz is $\approx$330 kΩ. For maximum effectiveness, Z_L should be of this order. rf compensation is effective against fluctuations of order $\tilde{V}_{\rm rf}$ if

$$Z_{L\ \rm eff} \gg Z_{s,x}\left(\frac{e|\tilde{V}_{\rm rf}|}{KT_e}-1\right). \tag{A2}$$

Figure 20 shows a sample calculation of this criterion for an electrode with $A_x=2$ cm^2 and inductors with $Z_L=250\,\mathrm{k}\Omega$ at 2 MHz. We have taken $|\tilde{V}_{\rm rf}|/T_e=30$ and $|V_s-V_p|/T_e=5$. This is the region near the floating potential where the nonlinearity of the $I-V$ curve is most severe. It is seen that an unaided probe cannot satisfy Eq. (A2), and a 2 cm^2 electrode is required to measure densities down to the mid-10^{10} cm^{-3} range.

Although in principle the electron energy distribution function (EEDF) can be found from the second derivative of the $I-V$ curve of a cylindrical probe, in practice a high degree of data smoothing is required to obtain this derivative. Furthermore, we see from Fig. 12 that the shape of the I_e-V curve depends on the quality of the ion subtraction. Nonetheless, several authors[24–26] have succeeded in obtaining interesting EEDF data with Langmuir probes. We regard these as exceptional *tours-de-force* by extraordinary experimentalists, rather than results that can be reproduced outside a dedicated laboratory. To measure the EEDF, one has to compute the second derivative of the $I-V$ curve, which can be done with adequate smoothing of the data. Another method is to use a dithered probe, whose voltage is modulated around V_p at a frequency low enough to pass the rf chokes, and with an amplitude small enough that the ion current does not change. Synchronous detection of the second harmonic should then yield d^2I/dV^2.

APPENDIX B: USE OF THE BOHM FORMULA FOR THIN SHEATHS

At high densities where the ion current is well saturated, it is common practice to use the Bohm formula of Eq. (4) to estimate the ion density, neglecting the expansion of the sheath. There is always a question of what probe voltage should be used for this reading, and what value of α should be used in the formula. In Fig. 21 we have generated artificial probe curves for a 3 eV argon plasma using the BRL theory with Maxwellian electrons, adjusting the density to give (a) $\xi=20$ and (b) $\xi=40$. Straight line extrapolations are drawn through the low- and high-voltage parts of the curves. The dashed line is the current predicted by Eq. (4), with the value of α adjusted to match the current extrapolated to the floating potential V_f. At $\xi=20$, it makes a difference which extrapolation is used, but the error is small with the more linear curve for $\xi=40$. The value of α, therefore, depends on ξ. This variation is shown in Fig. 22 for two practical cases: (a) when the ion current is measured at a constant offset of $25KT_e$ from V_f, and (b) when the ion curve is extrapolated to V_f. Note that this simple method of analysis works only when the BRL theory is applicable. If the $I-V$ characteristic has been distorted by collisions, it will not be linear enough for this method to give accurate results.

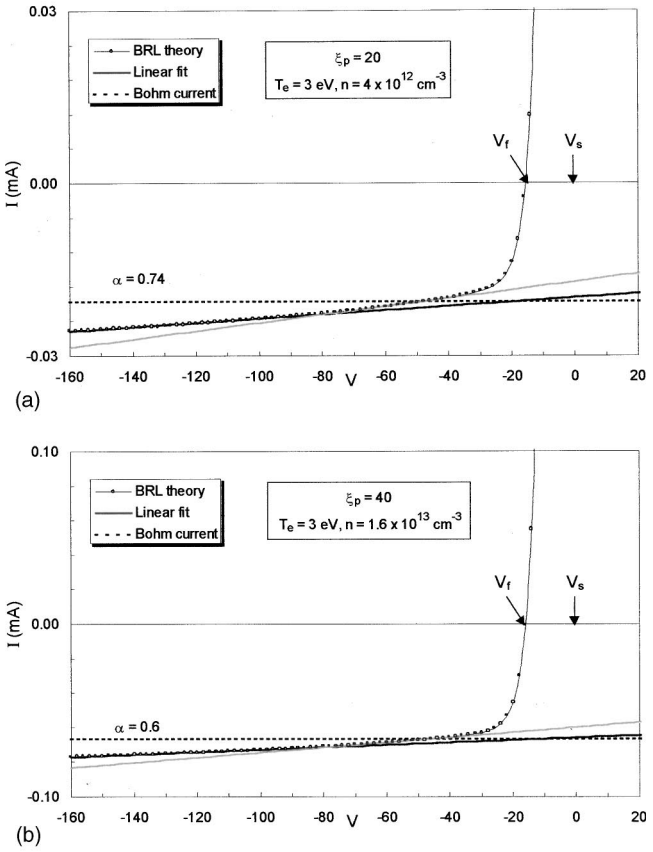

FIG. 21. BRL curves for a 3 eV argon plasma at densities corresponding to: (a) $\xi=20$ and (b) $\xi=40$. The straight lines are fitted to two regions of the ion saturation curve, and the dashed line is the current predicted by the Bohm formula with the stated value of the coefficient α.

The reason that ion curves do not reach a saturated value until ξ is on the order of 100 is that the sheath thickness at V_f is actually about $5\lambda_D$, and to this must be added the thickness of the Child–Langmuir (CL) sheath, which increases with $V_0^{3/4}=|V_p-V_s|^{3/4}$ and greatly increases the collection area. When the plane CL sheath thickness is evaluated with

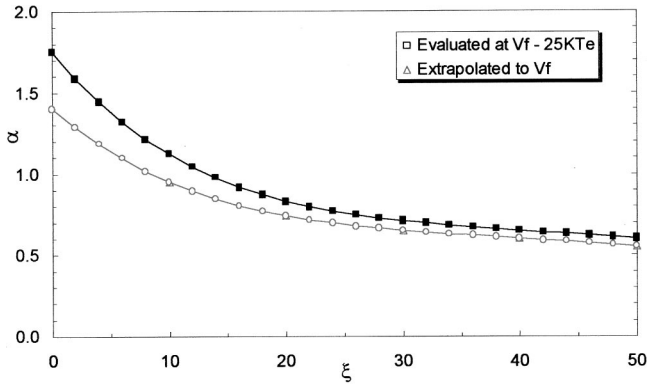

FIG. 22. Variation of the coefficient α with ξ for the use of the Bohm formula applied to the ion current: (a) measured at $V_f - 25KT_e$ (squares), or (b) extrapolated to V_f (diamonds).

the ion current set equal to the Bohm value, the total sheath thickness is given by[27]

$$d=\left[\frac{2}{3}\left(\frac{2eV_0}{KT_e}\right)^{3/4}+5\right]\lambda_D, \tag{B1}$$

where λ_D is evaluated with the plasma density, not the density at the sheath edge. Since the collection area increases with d in cylindrical geometry, I_i increases as $V_0^{3/4}$, as is often observed. Figure 23 is a plot of Eq. (B1) with and without the last term representing the Debye sheath. A simple fit to $I_i - V$ curves behaving as $V_0^{3/4}$ can be obtained by dividing the sheath into layers. Let the probe radius be a, the radius of the CL sheath be b, and let the normal Debye sheath edge be at $r=s$. Suppose we let b be the radius at which $V=V_f$. Then

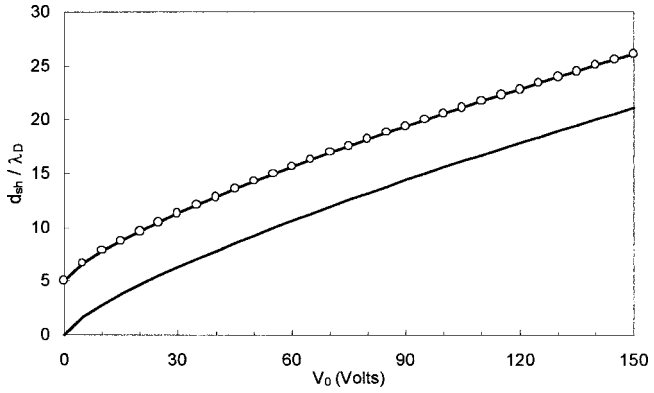

FIG. 23. Child–Langmuir sheath thickness vs probe potential, normalized to λ_D. The point include the Debye sheath thickness, whereas the line does not.

$$eV_b=KT_e\ln[(2M/\pi m)^{1/2}]\approx -5.4KT_e \tag{B2}$$

for argon. At the sheath edge s, the potential is $-0.5KT_e$ relative to the body of the plasma. Thus, in Eq. (B1) we should set $V_0=V_p-6KT_e/e$. The ion current is then

$$I_i=(d/a)I_B, \tag{B3}$$

where I_B is the Bohm current given by Eq. (4). The ABR theory, of course, gives the exact solution without dividing the sheath into layers, but this approach is simpler and not subject to deviations from the aymptotic behavior of the exact solution. A variation of this approximation was given by Hutchinson.[28] Godyak *et al.*[29] have pointed out that Eq. (21) should be modified for cylindrical geometry, but using the Langmuir–Blodgett corrections as quoted, for instance, by Chen[6] would defeat the simplicity of this method.

[1] H. M. Mott-Smith and I. Langmuir, Phys. Rev. **28**, 727 (1926).
[2] J. E. Allen, R. L. F. Boyd, and P. Reynolds, Proc. Phys. Soc. London, Sect. B **70**, 297 (1957).
[3] F. F. Chen, J. Nucl. Energy, Part C **7**, 47 (1965).
[4] I. B. Bernstein and I. N. Rabinowitz, Phys. Fluids **2**, 112 (1959).
[5] S. H. Lam, Phys. Fluids **8**, 73 (1965).
[6] F. F. Chen, in *Plasma Diagnostic Techniques*, edited by R. H. Huddlestone and S. L. Leonard (Academic, New York, 1965), Chap. 4, pp. 113–200.
[7] F. F. Chen, C. Etievant, and D. Mosher, Phys. Fluids **11**, 811 (1968).
[8] See National Technical Information Service Document No. AD634596 (University of Toronto Institute of Aerospace Studies Report No. 100 by J. G. Laframboise, June, 1966). Copies may be ordered from The National Technical Information Service, Springfield, VA.
[9] J. Virmont and R. Godard, Plasma Phys. **14**, 793 (1972).
[10] I. Cohen, Phys. Fluids **6**, 1492 (1963).
[11] P. M. Chung, L. Talbot, and K. J. Touryan, *Electric Probes in Stationary and Flowing Plasmas* (Springer, New York, 1975).
[12] P. C. Stangeby, J. Phys. D **15**, 1007 (1982).
[13] F. F. Chen, J. Appl. Phys. **36**, 675 (1965).
[14] C. Steinbrüchel, J. Vac. Sci. Technol. A **8**, 1663 (1990).
[15] A. Karamcheti and Ch. Steinbrüchel, J. Vac. Sci. Technol. A **17**, 3051 (1999).
[16] M. Mausbach, J. Vac. Sci. Technol. A **15**, 2923 (1997).
[17] A. A. Sonin, University of Toronto Institute of Aerospace Studies Report No. 109, 1965 (unpublished).
[18] M. B. Hopkins and W. G. Graham, Rev. Sci. Instrum. **57**, 2210 (1986).
[19] M. B. Hopkins, J. Res. Natl. Inst. Stand. Technol. **100**, 415 (1995).
[20] J. D. Evans, W. Zawalski, and F. F. Chen, Bull. Am. Phys. Soc. **45**, 146 (2000).
[21] M. E. Light (private communication, 2000).
[22] N. Hershkowitz, in *Plasma Diagnostics*, edited by O. Auciello and D. L. Flamm (Academic, London, 1989), Vol. 1, p. 113.
[23] I. D. Sudit and F. F. Chen, Plasma Sources Sci. Technol. **3**, 162 (1994).
[24] M. M. Turner and M. B. Hopkins, Phys. Rev. Lett. **69**, 3511 (1992).
[25] V. A. Godyak and V. I. Kolobov, Phys. Rev. Lett. **81**, 369 (1998).
[26] I. D. Sudit and R. C. Woods, Rev. Sci. Instrum. **64**, 2440 (1993).
[27] M. A. Lieberman and A. J. Lichtenberg, *Principles of Plasma Discharges and Materials Processing* (Wiley, New York, 1994), p. 165.
[28] I. H. Hutchinson, *Principles of Plasma Diagnostics* (Cambridge University Press, New York, 1987).
[29] V. A. Godyak, R. B. Piejak, and B. M. Alexandrovich, J. Appl. Phys. **73**, 3657 (1993).